Opto-Electronic Engineering

Article

2017, Vol 44, Issue 6

Generating HDR radiance maps from single LDR image

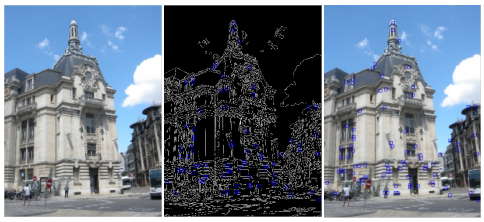

Xiaofen Li and Yongqing Huo*

School of Communications and Information Engineering, University of Electronic Science and Technology of China, Chengdu 611731, China

Abstract: We present a method of generating high dynamic range (HDR) radiance maps from a single low dynamic range (LDR) image and its camera response function (CRF). The method first models and estimates the inverse CRF and then multiplies the inverse CRF by a weighting function to make it smooth near the maximum and minimum pixel values, and finally conducts the smooth inverse CRF on the input LDR image to generate HDR image. In the method, the inverse CRF is estimated using one single LDR image and an empirical model of CRF, based on measured RGB distributions at color edges. Unlike most existing methods, the proposed method expands image from both high and low luminance regions. Thus, the algorithm can avoid the artifacts and detail loss in dark area which results from extending image only from bright region. Extensive experimental results show that the approach induces less contrast distortion and produces high visual quality HDR image.

Keywords: high dynamic range (HDR) image; low dynamic range (LDR) image; camera response function (CRF); image quality metric

DOI: 10.3969/j.issn.1003-501X.2017.06.002 **Citation:** *Opto-Elec Eng*, 2017, **44**(6): 577–586

1 Introduction

High dynamic range (HDR) imaging has attracted more and more attention not only from academia but also from industry. Researchers have proposed a number of methods to acquire HDR image. The most common one is multi-exposure, which captures multiple different exposure low dynamic range (LDR) images of the same scene and generates one HDR image by these images. However, the vast majority images captured in the last few decades only have one exposure. Thus, in recent years, researchers begin to focus on generating HDR image from single LDR image. They have made some progress and presented several algorithms. These algorithms can be classified into linear or nonlinear, global model or local model.

Daly and Feng [1,2] presented two methods for decontouring for high contrast displays, and these methods can generate medium dynamic range image and remove contouring in the transition areas, without particularly emphasizing on overexposed and underexposed areas. Landis [3] proposed one of global expansion methods, which is based on power function, and is used primarily for relighting digital three-dimensional models from images. Akyuz et al. [4] performed a series of psychophysical experiments to investigate how well LDR content is supported by HDR displays. The experiments were run to evaluate the effect of displaying tone mapped image, single exposure image, and HDR image on HDR screen. They suggested that linear expansion is competent for high-quality LDR images to displaying on HDR screen. Masia et al. [5] proposed another global method used for overexposed LDR images by gamma expansion. They conducted a study to predict the gamma value, in which users were asked to adjust manually the gamma value. This expansion method may fail to utilize the dynamic range to its full extent. Huo et al. [6] proposed an expansion method based on human vision system (HVS). This approach takes local luminance information into the global expansion using the local model of HVS.

For local methods, images are always classified into overexposed/non-overexposed areas or diffuse/specular parts, and different schemes are applied to expand each portion. Meylan et al. [7,8] and Didyk et al. [9] attempted to expand different regions of the LDR image by identifying or classifying the image into different parts such as highlights, and light sources etc. The main idea of Meylan et al. 's method is to detect the diffuse and specular parts of the image and to expand them using different linear functions. Didyk et al. [9] classified a scene into three components: diffuse, reflections, and light sources, and enhanced only reflections and light sources. This method is semiautomatic.

Received 12 March 2017; accepted 10 April 2017

* E-mail: hyq980132@uestc.edu.cn

Banterle et al. [10,11] and Rempel et al. [12] focused on dealing with overexposed areas using a guidance way to direct the expansion of these areas. Banterle et al. 's method uses an inverted tone mapping operator for expanding the dynamic range combined with a smooth field for the reconstruction of lost information in overexposed areas. This algorithm provides a general solution for visualization of LDR image on HDR monitors and IBL. Rempel et al. 's algorithm first removes artifacts, and then linearizes the signal using an inverse gamma function, and finally employs a brightness enhance function (BEF) to enhance brightness in highlight regions. Kovaleski and Oliveira [13] proposed an improvement version of Rempel et al. 's method, which accomplishes Gaussian blur and edge stopping by a bilateral filter.

Wang et al. [14] proposed a user-based approach, in which the texture of overexposed areas is repaired with similar clear texture in correct exposed areas. The whole process was termed hallucination, the first step is to linearize the signal, and then each overexposed region is detected and fitted with an elliptical Gaussian lobe. Huo et al. [15,16] first recovered the information in overexposed areas by highlight removal technique, and then expanded the image using a linear function.

The HDR image type is divided into single exposure HDR and multi-exposure HDR. The multi-exposure HDR uses many frames with different exposure time to fuse the HDR image, so the image fusion method is the key technology of HDR image. Guan et al. [17] proposed a HDR image fusion algorithm based on the Laplace Pyramid. They chose the fusion strategy based on regional average gradient for the top layer of the long exposure image and short exposure image and then the remained layers which represent the edge feature information are based on regional energy. Florea et al. [18] proposed a logarithmic type image processing (LTIP) model, the performing exposure merging under the LTIP model is equivalent to standard irradiance map fusion. Narahari et al. [19] provided a system to align and merge differently exposed digital images to create a HDR image. In the system, the captured image is operated in the hue-saturation-intensity (HIS) color space, the saturation component in the HSI color space is used to pick the color or purity of pixels and intensity channel is used to weigh the sharpness of pixels of each of the differently exposed captured images.

Most of existing algorithms focus on expanding the image only from highlight region, which may reduce the visible details in dark region. Furthermore, the existing ones do not take the imaging mechanism into consideration.

In this paper, we propose a method of HDR image generation from single LDR image. The algorithm is based on the estimated inverse camera response function (CRF) which maps the nonlinear color distributions of edge regions in LDR image into linear distributions in image irradiance. The main contributions of the proposed method consist in two aspects: the smoothness function used in the estimation of inverse CRF and the utilization of the inverse CRF in HDR image generation. The first one makes the estimated inverse CRF curve more smooth, thus takes full advantage of the correct exposed pixels and suppresses the over- and under- exposed pixels, and reduces the contour artifacts in HDR image. The second one inverse the imaging procedure to recover the HDR irradiance which makes the produced HDR image more nearly to natural scene.

The remainder of this paper is arranged as follows. Section 2 describes the proposed algorithm. The implementation details and extensive experimental results are discussed in Section 3. Conclusions are given in the last section.

2 Algorithm description

The proposed algorithm generates HDR image from single LDR image depending on inverse CRF reconstruction. The main steps include: inverse CRF estimation, inverse CRF smoothness, and HDR image generation. The approach first models and estimates inverse CRF based on the database established by Grossberg et al. [20], and then, smoothens the estimated inverse CRF by a weighting function, and finally, conducts the inverse CRF on the input LDR image to generate HDR image. The flowchart of the algorithm is shown in Fig. 1.

The sub sections 2.1 and 2.2 describe inverse CRF

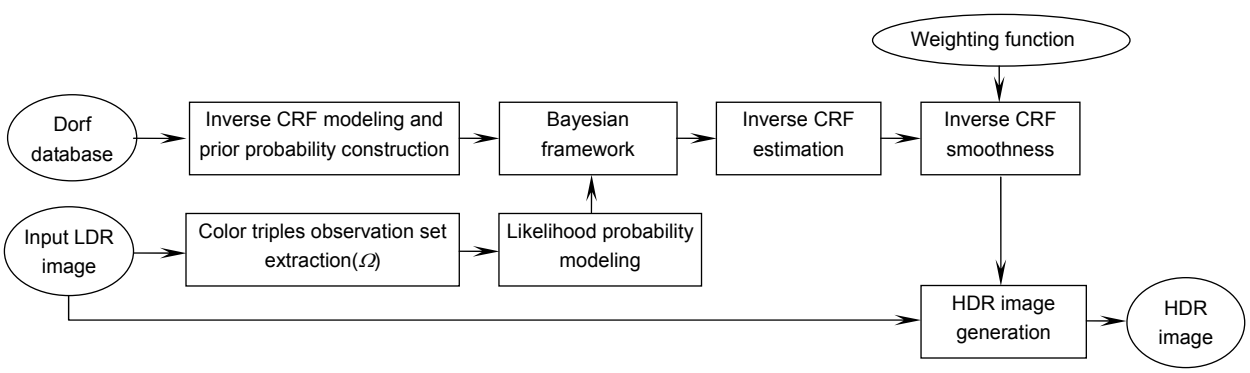

Fig. 1 The flowchart of the proposed method.

estimation, and sub section 2.3 represents inverse CRF smoothness and HDR image generation. The inverse CRF is reconstructed using the edge pixels in the LDR image based on the Grossberg's DoRF database and EMoR database [20], and the prior probability is empirically modeled as a Gaussian mixture model. Then, a Bayesian framework is formed by combining the likelihood function with the prior model. Finally, the optimal inverse CRF is obtained by maximizing the posteriori probability (MAP).

2.1 Edge color distributions

Because the inverse CRF is reconstructed using the edge pixels in the LDR image, the first step is to find and select the suitable edge blocks. The edge block includes three kinds of image intensities which is called edge triple colors. The radiometric response function f of imaging system maps the image irradiance I, which is linearly related to scene radiance to the measured intensity B in the image [21]:

$$B = f(I), \tag{1}$$

Since the CRF is a nonlinear function, the linearly distributed image irradiances in the edge regions are mapped into non-linear distributed image intensities. Thus, the inverse camera response function f_{inv} should transform the image intensities in the edge regions into values linearly related to image irradiance. That means $f_{\text{inv}}(B_p)$ should be on the line defined by $f_{\text{inv}}(B_1)$ and $f_{\text{inv}}(B_2)$, where B_p is the pixel value of the edge, B_1 and B_2 are pixel values of the regions divided by the edge. By detecting the eligible edge triple colors $\{B_1, B_2, B_p\}$ and modeling the total distance D from $f_{\text{inv}}(B_p)$ to the line $f_{\text{inv}}(B_1)f_{\text{inv}}(B_2)$, the inverse response function f_{inv} can be obtained through finding the optimal solution to minimize the total distance D:

$$\begin{aligned} D(f_{\text{inv}}, \Omega) &= \sum_{\Omega} \frac{\left| f_1(B) \times f_2(B) \right|}{\left| f_1(B) \right|}, \\ f_1(B) &= f_{\text{inv}}(B_1) - f_{\text{inv}}(B_2), \\ f_2(B) &= f_{\text{inv}}(B_p) - f_{\text{inv}}(B_2), \end{aligned} \tag{2}$$

Where "×" is the cross product between two vectors; Ω is the set of color triples. The edge is detected by Canny operator. Fig. 2 shows the detected edges and color triples of the input LDR image.

2.2 Inverse CRF estimation

To search the optimal solution for minimizing the total distance D, the inverse response function f_{inv} can be modeled as:

$$f_{\text{inv}} = f_{\text{inv0}} + C\boldsymbol{H}, \tag{3}$$

Where f_{inv0} is the mean inverse camera response of the CRFs in EMoR database, $\boldsymbol{H}$ is a matrix whose columns are composed of the first 5 eigenvectors of covariance matrix constructed by the inverse functions of the CRFs in EMoR database, and C is a coefficient matrix which can be optimized.

The prior probability $p(f_{\text{inv}})$ is modeled as a Gaussian mixture model using the 201 inverse response functions in DoRF database.

$$p(f_{\text{inv}}) = \sum \alpha_i N(f_{\text{inv}}; \mu_i, \Sigma_i). \tag{4}$$

The likelihood probability $p(f_{\text{inv}}/\Omega)$ is modeled by incorporating the total distance D into an exponential function:

$$p(\Omega \mid f_{\text{inv}}) = \frac{1}{Z} \exp[-\lambda D(f_{\text{inv}}; \Omega)]. \tag{5}$$

Where Z is a normalization constant, and λ is a variable parameter which will be discussed in the following.

With $p(f_{\text{inv}})$ and $p(f_{\text{inv}}/\Omega)$, we can formulate the problem in a Bayesian framework. The optimal inverse response function f_{inv}^* is solved as:

$$f_{\text{inv}}^* = \arg\max p(\Omega \mid f_{\text{inv}}) p(f_{\text{inv}}). \tag{6}$$

Taking the log of equation (6), f_{inv}^* can be written as:

$$f_{\text{inv}}^* = \arg\min \lambda D(f_{\text{inv}}; \Omega) - \log p(f_{\text{inv}}). \tag{7}$$

The optimal solution of f_{inv}^* is computed by the Levenberg-Marquardt method. PCA can be done by eigenvalue decomposition of a data covariance (or correlation) matrix or singular value decomposition of a data matrix. From equation (3), we know that when f_{inv0} and $\boldsymbol{H}$ are known, C is the only unknown coefficient matrix. So when using PCA dimension reduction model, we aim to compute the optimal PCA dimension reduction coefficient matrix C, other than the response function f_{inv}. For RGB image, three color channels can be treated separately,

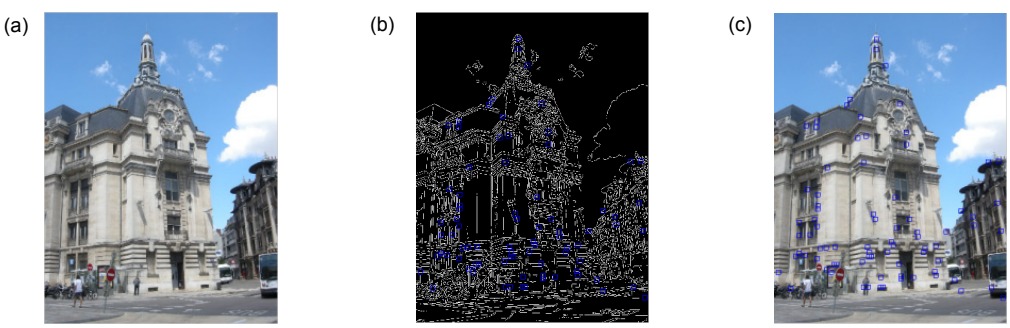

Fig. 2 Observation set of color triples. (a) Input image. (b) The detected edge and color triples. (c) The original image with color triples.

so the response functions of the RGB channels differ from each other. Fig. 3 shows an illustration of estimated inverse response function for RGB image with λ=1000.

In the experiment, we found that the value of λ influences the shape of inverse response function. From equation (7), it is obvious that the optimal solution of f_{inv}^* depends on the prior probability and the likelihood probability simultaneously. The parameter λ is used to balance the effect of the prior $p(f_{inv})$ and the likelihood $p(f_{inv}/\Omega)$ for function f_{inv}. When λ is larger, the optimal solution of f_{inv}^* will more rely on the likelihood probability. That is to say, f_{inv}^* depends on the samples from the input LDR image mostly, in this case, the f_{inv}^* is less smooth and sensitive to noise. On the contrary, when λ is smaller, f_{inv}^* depends on the prior model mostly and is more smooth. However, in this case, f_{inv}^* is not so good to approximate the real inverse CRF of the imaging device which captures the input LDR image. Thus, the selected λ

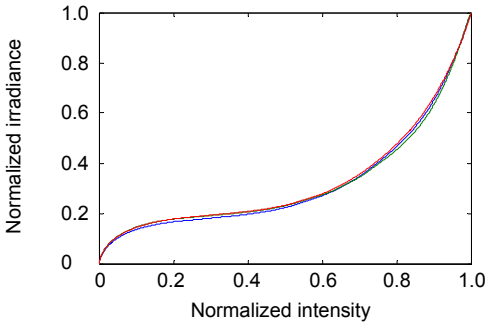

Fig. 3 The RGB inverse response curve estimated from the test image building.

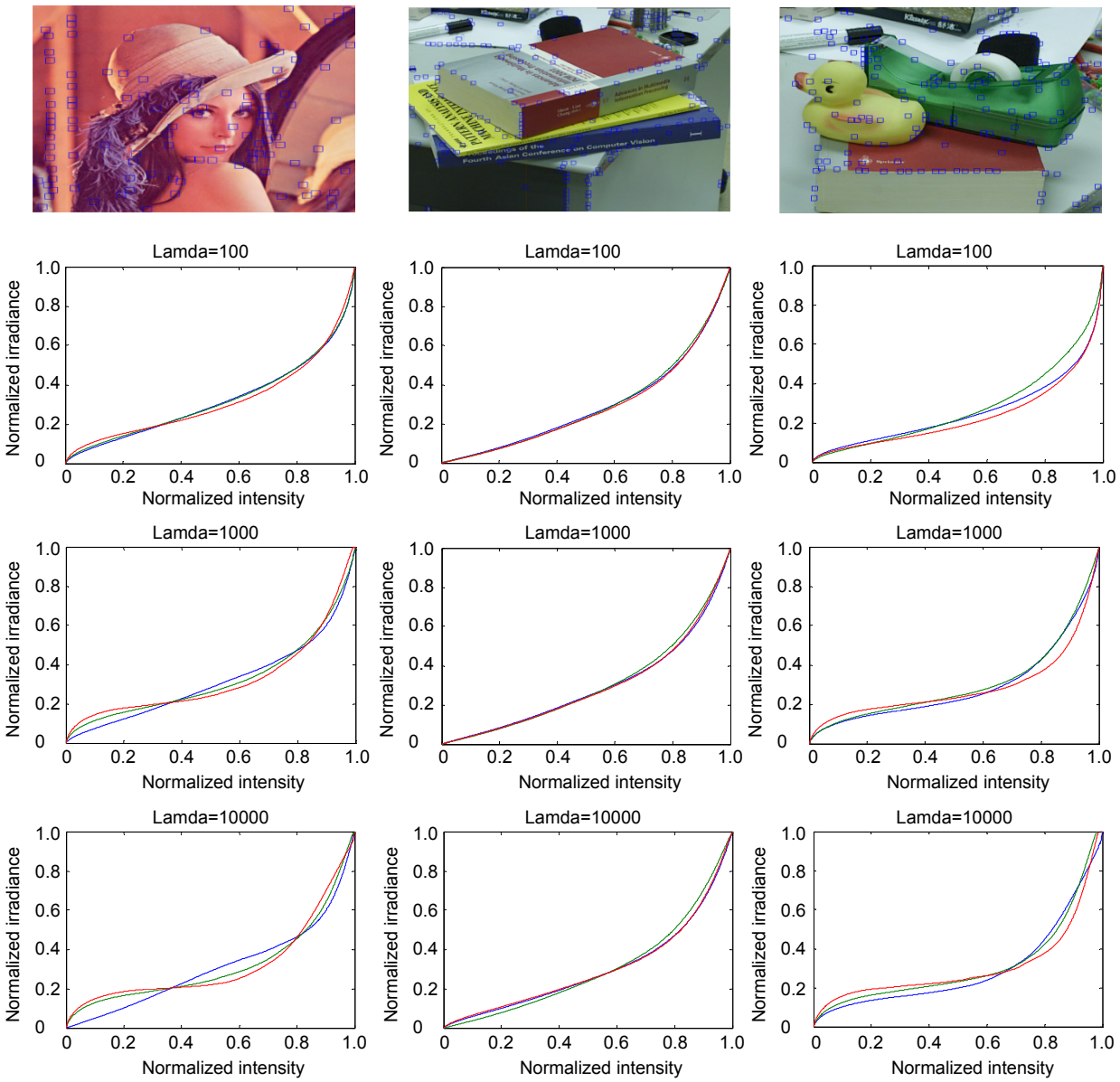

Fig. 4 The inverse response curve of input images with different λ values, from top to bottom: input image with edge detection, the curves with λ=100, λ=1000 and λ=10000.

value should be a trade-off between the effect of likelihood probability and prior model. We perform the experiments with λ=100, 1000 and 10000. Fig. 4 shows the results.

Fig. 4 shows the estimated inverse response functions with different λ values. When λ=100, the effect of image samples is less than that of prior model, it is obvious that the inverse response functions of RGB channels are bonding together. When λ=10000, the effect of image samples is more than that of prior model. The tendency of three inverse response functions are inconsonant. Taking the overall effect into consideration, through the experiments, we found that λ=1000 is more suitable in our experiments.

2.3 HDR image generation

The response function f is monotonic and invertible [22]. So rewrite the Equation (1) as:

$$I_i = f_{\text{inv}}(B_i), \tag{8}$$

Where i denotes pixel position. Letting $B_{\min}$ and $B_{\max}$ be the minimal and maximal pixel values, N be the number of pixels. Because the inverse function f_{inv} typically has a steep slope near $B_{\min}$ and $B_{\max}$, it is less smooth and non-monotonic near these extremes. To solve this problem, we introduce a weighting function $w(B)$ to make the function f_{inv} more smooth and reduce the effect of the pixels near $B_{\min}$ and $B_{\max}$ in HDR image construction. The considerable choices of $w(B)$ are Rectangular function, Triangular function and Gaussian function.

Triangular function is a simple hat function, defined as:

$$tri(t) = \max(1-|t|,0). \tag{9}$$

While applying to pixel values, the function can be transformed as follows:

$$w(B) = \begin{cases} m - B_{\min}, & \text{for} \quad m \le 0.5(B_{\min} + B_{\max}) \\ B_{\max} - m, & \text{for} \quad m > 0.5(B_{\min} + B_{\max}) \end{cases}. \tag{10}$$

Gaussian weighting function is defined as:

$$f(x \mid \mu, \sigma^2) = \frac{1}{\sqrt{2\pi}\cdot\sigma}\exp[-\frac{(x-\mu)^2}{2\sigma^2}]. \tag{11}$$

We use the normal function with μ=0 and σ=1, then scale the amplitude and move the symmetric function to the range of pixel value. Then the weighting function is:

$$\begin{cases} w(B) = \frac{1}{2}(B_{\min} + B_{\max})\cdot f(m \mid 0,1) \\ m = 6\cdot(\frac{m}{255} - 0.5) \end{cases}. \tag{12}$$

For rectangular function, the operation is simply equivalent to multiplying by a coefficient when recovering the high dynamic range irradiance maps. Fig. 5 shows the three kinds of weighting functions.

Combining equation (8) with the weighting function, we can easily recover high dynamic range irradiance values:

$$I_i = \frac{w(B_i)\cdot f_{\text{inv}}(B_i)}{\sum_{j=0}^{255} w(B_j)}. \tag{13}$$

3 Experimental evaluation

To evaluate the proposed algorithm, the method is compared with four inverse tone mapping operators, which are Banterle et al. 's ITM [11], Masia et al. 's gamma expansion [5], Meylan et al. 's PWL [7], and Rempel et al. 's LDR2HDR [12] respectively. A wide dynamic range of images are used as test data. Fig. 6 shows a subset of the test images.

3.1 Tone mapped versions

Because the limitation of medium, HDR images cannot be showed here directly. The generated HDR images are tone mapped by Reinhard et al. 's tone mapping operator [23] to compare the performance of the algorithms indirectly. Moreover, to analyse the performance of three weighting functions, the HDR images obtained using different weighting functions are also tone mapped and shown in Fig. 7. The metric results of HDR images obtained using different weighting functions are shown in Fig. 8. The tone mapped images of five schemes are shown in Fig. 9.

3.2 Image quality metric results

To assess the performance of five compared methods, a

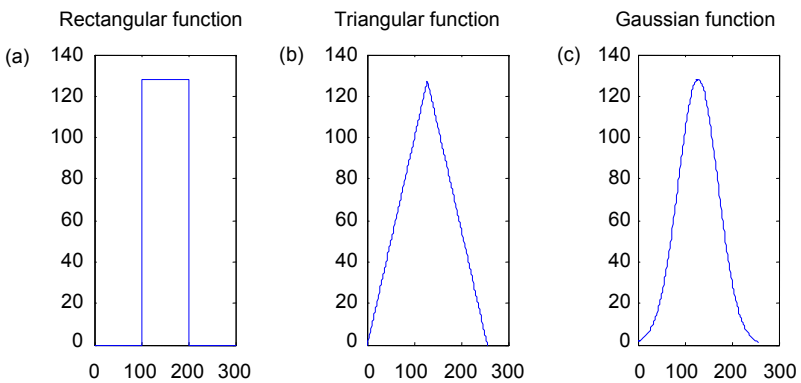

Fig. 5 Three kinds of weighting functions. (a) Rectangular. (b) Triangular. (c) Gaussian.

novel image quality metric introduced by Adyin et al. [24] is chosen to verify the quality of generated HDR images. This metric identifies distortions between two images, independently of their respective dynamic ranges. The metric uses a model of the human visual system, and classifies visible changes between a reference and a compared image. The result image generated by the metric is a summary image with red, green and blue pixels. The authors identify that red pixels mean reversal of visible contrast (when contrast polarity is reversed in the compared image with respect to the reference image). Green pixels imply loss of visible contrast (when visible contrast in the reference image becomes invisible in the compared image). Blue pixels denote amplification of invisible contrast (when invisible contrast in the reference image becomes visible in the compared image). Less blue pixels mean few contour artifacts produced during expansion. Furthermore, the less green and red pixels indicate the better performance of the algorithm. The metric parameters are set to the default values: typical LCD, viewing distance of 0.5 m, pixel per visual degree 30, and peak contrast 0.0025.

Fig. 6 Test images. (a) Farm road. (b) Tree. (c) Structure. (d) Tower. (e) Lake. (f) Statue. (g) Path. (h) Library. (i) Temple. (j) Ancient town. (k) Passageway. (l) Building. (m) Sunset. (n) Sunflower. (o) Teaching building.

Fig. 7 The tone mapped versions of HDR images generated by the proposed method with different weighting functions. (a) The tone mapped image with rectangular weighting function. (b) The tone mapped image with triangular weighting function. (c) The tone mapped image with Gaussian weighting function.

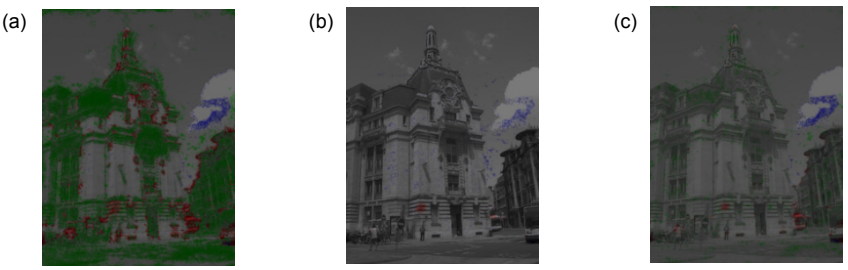

Fig. 8 The resulting metric images of the HDR images with different weighting functions. (a) Rectangular weighting function. (b) Triangular weighting function. (c) Gaussian weighting function.

In the comparison, the original LDR images and the produced HDR images are used as reference images and compared images respectively. To assess the performance of three weighting functions, the metric results of HDR images obtained using different weighting functions are shown in Fig. 8. Meanwhile, a part of metric images of five algorithms are shown in Fig. 10.

Moreover, we use the image quality evaluation indexes, such as PSNR (Peak Signal to Noise Ratio) and SSIM (Structural Similarity Index), to evaluate the performance of HDR images in Table 1. PSNR is most commonly used to measure the quality of reconstruction image, and SSIM

Fig. 9 The tone mapped images of compared methods. The original LDR images are (a) structure, (b) teaching building, (c) tower, (d) lake, (e) library and (f) temple.

Table 1 HDR image evaluation by PSNR and SSIM.

	Structure		Teaching building		Ancient town		Sunflower		Farm road	
	PSNR/dB	SSIM/%	PSNR/dB	SSIM/%	PSNR/dB	SSIM/%	PSNR/dB	SSIM/%	PSNR/dB	SSIM/%
Banterle	60.9	40.6	61.2	37.5	61.4	81.6	106.4	53.1	67.0	80.6
Masia	56.6	40.5	63.7	38.8	67.1	82.6	112.9	56.1	72.1	79.8
Meylan	65.1	30.8	59.3	38.7	62.9	80.3	44.2	40.9	78.9	80.5
Rempel	54.7	39.3	60.2	39.9	59.9	81.8	67.7	54.9	67.9	80.0
Ours	**70.4**	**42.1**	**87.3**	**49.9**	**145.3**	**85.6**	**118.9**	**57.6**	**142.4**	**84.2**

is used for measuring the similarity between two images. Meanwhile, to analyze the introduced distortion of each scheme more intuitively, the percentages of red pixels, green pixels, and blue pixels in metric images are computed and displayed in Table 2.

3.3 Result analyses and discussion

From Fig. 7, we note that the tone mapped image in Fig. 7(b) has more details both in the dark and bright regions than other two tone mapped images. That means the triangle weighting function is the best one in three functions. Fig. 8 also indicates the same conclusion. The resulting metric image in Fig. 8(b) has less green and red pixels compared to other two metric images. This turns out that the triangle weighting function introduces less contrast distortion than other two weighting functions.

Because of using the same tone mapped operator, the quality of the tone mapped images indirectly represents that of the corresponding HDR images. From Fig. 9, referring to the original LDR images, we find that Banterle et al.'s method has better performance in bright regions and bad performance in dark areas. The methods by Masia, Rempel and Meylan do slightly well in dark regions than in bright regions. Our proposed method works well and has better visual quality both in dark and bright regions. In Fig. 9, some of the tone mapped versions of Masia et al. 's algorithm have obvious artifacts in highlight areas. This results from the small key value of the input LDR image. In brief, the tone mapped versions of HDR images generated by our method has better visibility than that of other methods.

In Fig. 10, considering the six resulting metric images of each algorithm, each one of our metric images has very few red, green and blue pixels. That means our method induces minimum contrast distortion and fidelity loss. According to the metric, the less total pixels of red, green and blue indicate the better performance of the algorithm. We conclude that the general performance of our method is better than other compared algorithms. This is proved by the numerical results in Table 2.

We compare the HDR image quality with two classical and practical quality metrics, including PSNR and SSIM in Table 1. The reference images are the 5 single input images, and the test images are the tone mapped images from HDR images using the same tone mapping operator, while the HDR images generated from our method and the four compared methods. For PSNR and SSIM, a higher PSNR generally indicates that the reconstruction

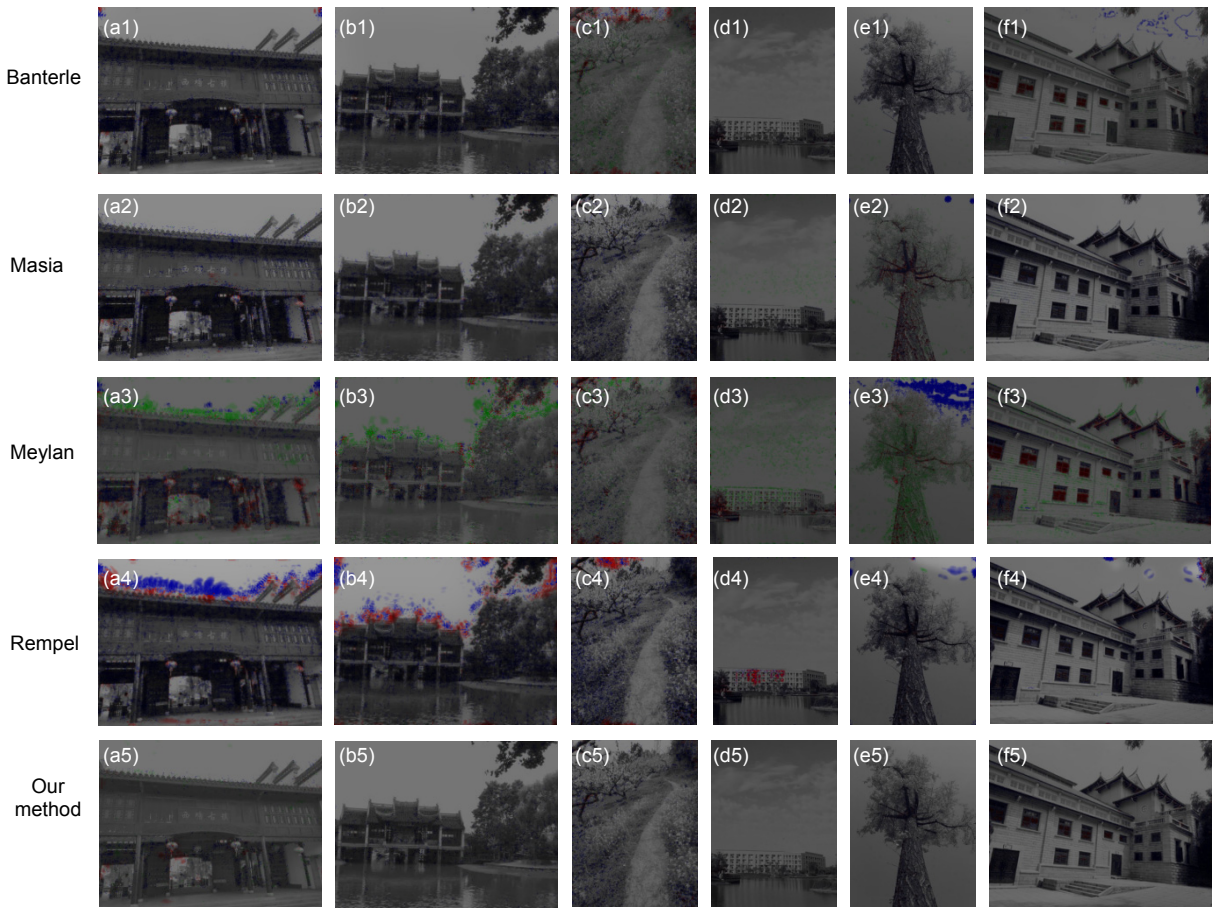

Fig. 10 The metric results. (a) The original LDR images are ancient town. (b) Building. (c) Farm road. (d) Structure. (e) Tree. (f) Teaching building.

is of higher quality, and also a higher SSIM means the higher similarity of two images. From Table 1, we found that our method has both highest PSNR and SSIM between five methods.

Table 2 shows the contrast distortion percentage of metric results on 15 test images. Considering the number of the smallest values for each kind of contrast distortion, from Table 2, we can see that, for reversal of visible contrast, the orders of the performance from the best to the worst are Masia, our method, Banterle, Meylan and Rempel. For loss of visible contrast, the method of Banterle is the best, followed by Rempel, our method,

Table 2 Contrast distortion comparison. %

	Ancient town				Passageway				Building			
	Reverse	Loss	Amplification	Total	Reverse	Loss	Amplification	Total	Reverse	Loss	Amplification	Total
Banterle	**2.6**	1.5	29.5	33.6	3.5	**1.3**	17.9	22.7	1.1	**0.9**	23.7	25.7
Masia	4.1	3.2	34.9	42.2	**1.6**	2.6	27.5	31.6	1.3	1.3	35.2	37.7
Meylan	11.8	19.9	23.9	55.6	9.9	14.7	10.9	35.6	5.9	16.0	10.3	32.2
Rempel	10.6	**1.0**	57.9	69.6	11.9	1.3	31.2	44.4	12.1	1.5	49.5	63.1
Ours	3.7	4.6	**6.1**	**14.4**	4.2	3.5	**6.7**	**14.5**	**0.2**	1.1	**8.4**	**9.6**
	Sunset				Sunflower				Farm road			
	Reverse	Loss	Amplification	Total	Reverse	Loss	Amplification	Total	Reverse	Loss	Amplification	Total
Banterle	0.6	0.9	45.5	47.0	0.2	1.0	10.5	11.7	8.6	17.2	**3.9**	29.6
Masia	**0.5**	1.1	49.4	51.0	0.8	9.2	13.1	23.0	**1.5**	1.8	29.4	32.7
Meylan	1.7	5.9	39.4	47.0	1.2	23.3	4.0	28.5	8.4	14.4	11.5	34.3
Rempel	2.6	**0.6**	67.1	70.3	0.5	0.9	12.9	14.2	5.0	**1.5**	37.1	43.6
Ours	0.9	22.1	**17.8**	**40.8**	**0.0**	**0.9**	**2.0**	**2.9**	2.0	1.6	19.5	**23.2**
	Tree				Structure				Teaching building			
	Reverse	Loss	Amplification	Total	Reverse	Loss	Amplification	Total	Reverse	Loss	Amplification	Total
Banterle	1.5	4.7	39.0	45.2	0.8	**0.2**	11.3	12.3	4.5	9.7	19.2	33.4
Masia	9.6	24.4	**10.8**	44.9	0.7	14.9	15.2	30.8	**1.8**	3.6	50.4	55.8
Meylan	7.5	39.9	15.1	62.6	3.8	46.1	**4.1**	54.0	9.0	33.0	**16.0**	58.0
Rempel	2.2	1.0	37.9	41.1	2.7	0.3	15.2	18.2	2.7	0.7	41.7	45.0
Ours	**1.5**	**0.6**	26.5	**28.7**	**0.7**	0.6	8.8	**10.1**	1.9	**0.4**	30.2	**32.4**
	Tower				Lake				Statue			
	Reverse	Loss	Amplification	Total	Reverse	Loss	Amplification	Total	Reverse	Loss	Amplification	Total
Banterle	3.4	0.2	47.4	51.1	**0.5**	**0.1**	29.2	29.8	1.6	**0.4**	50.9	53.0
Masia	3.7	0.9	52.7	57.4	1.2	2.7	31.3	35.2	**1.2**	1.4	61.7	64.3
Meylan	10.2	6.0	40.7	56.9	2.4	15.7	19.4	37.5	14.3	16.4	39.5	70.1
Rempel	5.0	**0.2**	55.5	60.7	2.5	0.2	41.8	44.5	4.2	0.3	63.4	68.0
Ours	**2.4**	1.0	**38.8**	**42.2**	1.1	8.5	**11.7**	**21.4**	3.3	7.8	**28.8**	**39.9**
	Library				Temple				Path			
	Reverse	Loss	Amplification	Total	Reverse	Loss	Amplification	Total	Reverse	Loss	Amplification	Total
Banterle	2.8	4.4	55.8	63.0	4.1	**0.4**	45.3	49.8	6.1	0.5	50.0	56.6
Masia	**1.8**	3.9	31.1	36.8	**2.7**	4.3	57.2	64.1	**3.6**	3.2	69.3	76.0
Meylan	8.8	22.3	18.5	49.6	20.6	23.0	**31.6**	75.2	17.3	16.1	27.7	61.2
Rempel	2.4	**0.3**	38.4	41.1	6.9	0.5	54.3	61.6	7.5	**0.2**	65.0	72.7
Ours	3.3	4.5	**18.3**	**26.1**	4.7	3.0	36.4	**44.1**	9.8	7.7	**24.2**	**41.7**

Masia and Meylan. For amplification of invisible contrast, our method is the best, and the method of Meylan is the second, followed by Banterle, Masia and Rempel. For total contrast distortion, our method is the best, followed by Banterle, Masia, Meylan and Rempel.

4 Conclusions

In this paper, we present a method for producing HDR image by estimating and performing the inverse CRF on single LDR image. We construct the model of inverse CRF according to the monotonic property of camera response function and its database, estimate the inverse CRF by establishing Bayesian framework and solving the maximum of the posteriori probability, and produce HDR image by weighting and conducting the inverse CRF on single LDR image. Compared with other methods, our method induces the smallest contrast error and expands the dynamic range from both highlight area and shaded region. The performance of the estimated inverse CRF affects the HDR image quality. In the future work, we will explore more high-performance scheme for reconstructing the inverse camera response function.

Acknowledgements

This work was supported by the National Natural Science Foundation of China (61401072).

References

1 Daly S J, Feng Xiaofan. Bit-depth extension using spatiotemporal microdither based on models of the equivalent input noise of the visual system[J]. *Proceedings of SPIE*, 2003, **5008**: 455–466.

2 Daly S J, Feng Xiaofan. Decontouring: prevention and removal of false contour artifacts[J]. *Proceedings of SPIE*, 2004, **5292**: 130–149.

3 Landis H. Production-ready global illumination[C]// SIGGRAPH Course Notes 16, 2002: 87–101.

4 Akyüz A O, Fleming R, Riecke B E, *et al*. Do HDR displays support LDR content?: a psychophysical evaluation[J]. *ACM Transactions on Graphics* (*TOG*), 2007, **26**(3): 38.

5 Masia B, Agustin S, Fleming R W, *et al*. Evaluation of reverse tone mapping through varying exposure conditions[J]. *ACM Transactions on Graphics* (*TOG*), 2009, **28**(5): 160.

6 Huo Yongqing, Yang Fan, Dong Le, *et al*. Physiological inverse tone mapping based on retina response[J]. *The Visual Computer*, 2014, **30**(5): 507–517.

7 Meylan L, Daly S, Süsstrunk S. The reproduction of specular highlights on high dynamic range displays[C]// 14th Color and Imaging Conference Final Program and Proceedings, 2006: 333–338.

8 Meylan L, Daly S, Süsstrunk S. Tone mapping for high dynamic range displays[J]. *Proceedings of SPIE*, 2007, **6492**: 649210.

9 Didyk P, Mantiuk R, Hein M, *et al*. Enhancement of Bright Video Features for HDR Displays[J]. *Computer Graphics Forum*, 2008, **27**(4): 1265–1274.

10 Banterle F, Ledda P, Debattista K, *et al*. Inverse tone mapping[C]// Proceedings of the 4th International Conference on Computer Graphics and Interactive Techniques in Australasia and Southeast Asia, 2006: 349–356.

11 Banterle F, Ledda P, Debattista K, *et al*. A framework for inverse tone mapping[J]. *The Visual Computer*, 2007, **23**(7): 467–478.

12 Rempel A G, Trentacoste M, Seetzen H, *et al*. LDR2HDR: on-the-fly reverse tone mapping of legacy video and photographs[J]. *ACM Transactions on Graphics* (*TOG*), 2007, **26**(3): 39.

13 Kovaleski R P, Oliveira M M. High-quality brightness enhancement functions for real-time reverse tone mapping[J]. *The Visual Computer*, 2009, **25**(5–7): 539–547.

14 Wang Lvdi, Wei Liyi, Zhou Kun, *et al*. High dynamic range image hallucination[C]// Proceedings of the 18th Eurographics conference on Rendering Techniques, 2007: 321–326.

15 Huo Yongqing, Yang Fan, Brost V, *et al*. LDR image to HDR image mapping with overexposure preprocessing[J]. *IEICE Transactions on Fundamentals of Electronics*, *Communications and Computer Sciences*, 2013, **E96**.**A**(6): 1185–1194.

16 Huo Yongqing, Yang Fan. High-dynamic range image generation from single low-dynamic range image[J]. *IET Image Processing*, 2016, **10**(3): 198–205.

17 Guan Wen, Li Li, Jin Weiqi, *et al*. Research on HDR image fusion algorithm based on Laplace pyramid weight transform with extreme low-light CMOS[J]. *Proceedings of SPIE*, 2015, **9675**: 967524.

18 Florea C, Vertan C, Florea L. High dynamic range imaging by perceptual logarithmic exposure merging[J]. *International Journal of Applied Mathematics and Computer Science*, 2015, **25**(4): 943–954.

19 Narahari N K, Bhat R, Vijaya R, *et al*. System and method to align and merge differently exposed digital images to create a HDR (High Dynamic Range) image: US20160125630[P]. 2016-05-05.

20 Grossberg M D, Nayar S K. What is the space of camera response functions?[C]// Proceedings of 2003 IEEE Computer Society Conference on Computer Vision and Pattern Recognition, 2003, **2**: II-602-9.

21 Lin S, Gu Jinwei, Yamazaki S, *et al*. Radiometric calibration from a single image[C]// Proceedings of the 2004 IEEE Conference on Computer Vision and Pattern Recognition, 2004, **2**: II-938–II-945.

22 Debevec P E, Malik J. Recovering high dynamic range radiance maps from photographs[C]// Proceedings of the 24th annual conference on Computer graphics and interactive techniques, 1997: 369–378.

23 Reinhard E, Stark M, Shirley P, *et al*. Photographic tone reproduction for digital images[J]. *ACM Transactions on Graphics* (*TOG*), 2002, **21**(3): 267–276.

24 Aydin T O, Mantiuk R, Myszkowski K, *et al*. Dynamic range independent image quality assessment[J]. *ACM Transactions on Graphics* (*TOG*), 2008, **27**(3): 69.